ELSEVIER

International Journal of Heat and Fluid Flow 23 (2002) 426–440

International Journal of HEAT AND FLUID FLOW

www.elsevier.com/locate/ijhff

Direct numerical simulation of turbulent concentric annular pipe flow Part 1: Flow field

Seo Yoon Chung [a], Gwang Hoon Rhee [b], Hyung Jin Sung [a,*]

[a] *Department of Mechanical Engineering, Korea Advanced Institute of Science and Technology, 373-1 Kusong-dong, Yusong-ku, Taejon 305-701, South Korea*

[b] *Department of Mechanical and Information Engineering, The University of Seoul, 90 Jeonnong-dong, Dongdaemun-gu, Seoul 130-743, South Korea*

Received 27 April 2001; accepted 25 December 2001

Abstract

A direct numerical simulation is performed for a turbulent concentric annular pipe flow at $Re_{D_h} = 8900$ for two radius ratios ($R_1/R_2 = 0.1$ and 0.5). Main emphasis is placed on the transverse curvature effect on near-wall turbulent structures. Near-wall turbulent structures close to the inner and outer walls are scrutinized by computing the lower-order and higher-order statistics. The Reynolds stress budgets are illustrated to confirm the results of the lower-order statistics. A quadrant analysis of the Reynolds shear stress is explored to develop a sufficiently complete picture of the contribution of flow events to turbulence production (consumption). Probability density functions of the inclination angles of the projected vorticity vectors are investigated to analyze the transverse curvature effects on the orientation of the vorticity field. The present numerical results show that the turbulent structures near the outer wall are more activated than those near the inner wall, which may be attributed to the different vortex regeneration processes between the inner and outer walls.

Keywords: Direct numerical simulation; Concentric annular pipe; Transverse curvature; Near-wall turbulent structure

1. Introduction

Annular pipe flow is important in engineering applications such as heat exchangers, gas-cooled nuclear reactors and drilling operations in the oil and gas industry (Nouri et al., 1993; Escudier et al., 1995). Also, annular pipe flow provides insight into the general problem of fully developed turbulent shear flows. In the case of a concentric annular pipe flow, two boundary layers exist which have different distributions of turbulent quantities. Moreover, pipe and channel flows are the limiting cases of annular pipe flow. For a small (high) radius ratio, the profiles of turbulent quantities close to the inner cylinder are similar to those of the TBL (turbulent channel flow) on a cylinder in an axial flow. On the other hand, the profiles close to the outer wall are similar to those of turbulent pipe flow in both cases.

A literature survey reveals that there have been many experimental and numerical studies on fully developed turbulent flow through concentric annuli (Knudsen and Katz, 1950; Brighton and Jones, 1964; Quarmby, 1967; Rehme, 1974). It is known that the main concern in the earlier experimental studies was the coincidence of the radial positions between zero shear stress and maximum velocity. Knudsen and Katz (1950), Brighton and Jones (1964) and Quarmby (1967) found that the radial position of maximum velocity is coincident with the position of zero shear stress. On the other hand, Rehme (1974) observed the non-coincidence of the positions between zero shear stress and maximum velocity through an intensive experimental work. Moreover, he found that the position of zero shear stress is closer to the inner wall than that of maximum velocity. Nouri et al. (1993) and Escudier et al. (1995) performed an LDV experiment in concentric annuli for a radius ratio ($\alpha = 0.5$). They used non-Newtonian fluids to take into account realistic flow characteristics. Azouz and Shirazi (1998) evaluated several turbulent models to predict the turbulent flow in

* Corresponding author. Tel.: +82-42-869-3027; fax: +82-42-869-5027.

E-mail address: hjsung@kaist.ac.kr (H.J. Sung).

0142-727X/02/$ - see front matter
PII: S0142-727X(02)00140-6

Nomenclature

C_f skin friction coefficient $= \tau_w/(1/2)\rho U_m^2$
D_h hydraulic diameter $= 4\delta$
F flatness factor
$F(v_r')$ flatness factor of the wall-normal velocity fluctuation
k turbulent kinetic energy $= (1/2)(\overline{v_r'^2} + \overline{v_\theta'^2} + \overline{v_z'^2})$
K_p non-dimensional pressure gradient $= \nu/(\rho u_\tau^3)\,\mathrm{d}p/\mathrm{d}z$
K^* energy partition parameter $= 2\overline{v_z'^2}/(\overline{v_r'^2} + \overline{v_\theta'^2})$
L_z computational length in the z direction
$L_{\theta_i}, L_{\theta_o}$ computational length of the inner and outer walls in the θ direction, respectively
N_r, N_θ, N_z grid points in the r, θ, z directions, respectively
p pressure
q_r, q_θ, q_z $q_\theta = v_\theta$, $q_r = r v_r$, $q_z = v_z$
r, θ, z spatial coordinates in the r, θ, z directions, respectively
R_1, R_2 radius of inner and outer cylinder, respectively
Re Reynolds number based on characteristic velocity and length scales
Re_δ Reynolds number $= U_c\delta/\nu$
Re_τ Reynolds number $= u_\tau\delta/\nu$
Re_{D_h} Reynolds number $= U_m D_h/\nu$
$R_{uu}(z)$ two-point correlations of fluctuating streamwise velocities in the z direction
$R_{uu}(\theta)$ two-point correlations of fluctuating streamwise velocities in the θ direction
S_{ij} mean strain rate tensor
$S(v_r')$ skewness factor of the wall-normal velocity fluctuation
t time
u_τ friction velocity $= (\tau_w/\rho)^{1/2}$
U_c laminar maximum velocity
U_m bulk mean velocity
v_r, v_θ, v_z velocity components in the r, θ, z directions, respectively
V_r, V_θ, V_z mean velocity components in the r, θ, z directions, respectively
y distance from the inner or outer wall

Greeks

α radius ratio $= R_1/R_2$
δ half width between inner wall and outer wall
Δr_i, Δr_o minimum grid spacing from the inner and outer wall, respectively
Δr_{max} maximum grid spacing in the radial direction
$\Delta\theta$, Δz grid spacing in the azimuthal and axial directions, respectively
ϵ dissipation rate of k
ν kinematic viscosity
ρ density of fluid
τ_w statistically averaged wall shear stress at the inner or outer wall
Θ inclination angle of projected vorticity vector $= \tan^{-1}(\omega_r/\omega_z)$
ω_r, ω_θ, ω_z fluctuating vorticity components in the r, θ, z directions, respectively

Abbreviations

CFL Courant–Friedrichs–Lewy
DNS direct numerical simulation
DS dissipation
KMM Kim, Moin and Moser
LDV laser Doppler velocimetry
PD pressure diffusion
p.d.f.s probability density functions
PR production
PS pressure strain
Q1,Q2,Q3,Q4 first, second, third and fourth quadrant, respectively
r.m.s. root mean square
TBL turbulent boundary layer
TD turbulent diffusion
VD viscous diffusion
VPG velocity–pressure gradient

Superscripts and subscripts

$(\ )'$ fluctuating component
$(\ )^+$ normalized by u_τ and ν
$^\circ$ angle in degree
$\overline{(\ )}$ statistically averaged in time and space
$(\ )_i$, $(\ )_o$ values of inner and outer walls, respectively
$(\ )_{rms}$ r.m.s. value
$\langle\ \rangle$ spatially averaged on the θ–z plane

concentric annuli. Their predicted results were compared with the experimental data of Nouri et al. (1993).

A perusal of the relevant literature indicates that studies of turbulent concentric annular pipe flows with transverse curvature are relatively scarce. By changing the radius ratio ($\alpha = R_1/R_2$), overall characteristics of the wall bounded turbulent structure in the vicinity of the inner and outer walls are altered significantly due to the influence of transverse curvature. Recently, Satake and Kawamura (1993) performed a large eddy simulation of concentric annular pipe flows with three radius ratios ($\alpha = 0.02$, 0.04 and 0.1). They focused on the identification of vortical structures near the inner wall. For a small radius ratio, turbulent structures near the inner wall are quite similar to those of TBL on a cylinder in an axial flow (Quarmby, 1967; Jonsson and

Sparrow, 1966). Neves et al. (1994) and Shin and Choi (2000) performed DNSs of axial flow boundary layers on cylinders. They considered the model problems as axial flows between concentric cylinders driven by mild streamwise pressure gradients in order to avoid difficulties with simulating spatially evolving boundary layers. Neves et al. (1994) showed that the slope of the mean velocity profile in the logarithmic region, turbulent intensities and Reynolds shear stress decrease as curvature increases. They also presented an energy partition parameter (K^*) to explain lower intercomponent energy transfer with increasing curvature. On the other hand, as opposed to those near the inner wall, the turbulent structures near the outer wall seem to be similar to those in pipe flow in the case of a small radius ratio.

The objective of the present study is to elucidate the transverse curvature effect on near-wall turbulent structure in concentric annular pipe flow. Toward this end, a DNS is performed for a turbulent concentric annular pipe flow. A schematic diagram and a coordinate system of the flow configuration are shown in Fig. 1. The transverse curvature effect on near-wall turbulent structure is analyzed for two radius ratios ($\alpha = 0.1$ and 0.5), which exemplify the situations of strong and weak curvature effects. The Reynolds number based on the bulk velocity (U_m) and the hydraulic diameter (D_h) is $Re_{D_h} = 8900$. A fractional step method with an implicit velocity decoupling procedure is employed to simulate the flow (Kim et al., 2002). This method is validated by testing a DNS of turbulent pipe flow. Lower-order and higher-order statistics are obtained to analyze the near-wall turbulent structures close to the inner and outer walls, which are compared with the previous DNS data of Kim et al. (1987), Eggels et al. (1994) and Neves et al. (1994). The Reynolds stress budgets are computed to confirm the results of the lower-order statistics. A quadrant analysis of the Reynolds shear stress is performed to obtain detailed information on the contribution to turbulence PR (consumption) from various flow events. The inclination angles of the projected vorticity vectors are examined by p.d.f.s to analyze the transverse curvature effects on the orientation of the vorticity field.

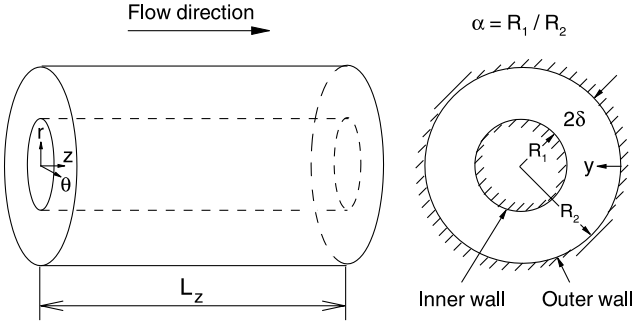

Fig. 1. Schematic diagram and coordinate system.

2. Equations and numerical procedure

In cylindrical coordinates, when the variables $q_\theta = v_\theta$, $q_r = rv_r$ and $q_z = v_z$ are introduced, the continuity equation is

$$\frac{1}{r}\frac{\partial q_r}{\partial r} + \frac{1}{r}\frac{\partial q_\theta}{\partial \theta} + \frac{\partial q_z}{\partial z} = 0. \tag{1}$$

Here, v_θ, v_r and v_z denote the azimuthal, radial, and axial velocity components, respectively. The Navier–Stokes equations in terms of the variables can be written as:

$$\begin{aligned}
\frac{Dq_\theta}{Dt} &= -\frac{1}{r}\frac{\partial p}{\partial \theta} + \frac{1}{Re}\left[\frac{1}{r}\left(\frac{\partial}{\partial r} r \frac{\partial q_\theta}{\partial r}\right) - \frac{q_\theta}{r^2} + \frac{1}{r^2}\frac{\partial^2 q_\theta}{\partial \theta^2} + \frac{\partial^2 q_\theta}{\partial z^2} + \frac{2}{r^3}\frac{\partial q_r}{\partial \theta}\right], \\
\frac{Dq_r}{Dt} &= -r\frac{\partial p}{\partial r} + \frac{1}{Re}\left[r\frac{\partial}{\partial r}\left(\frac{1}{r}\frac{\partial q_r}{\partial r}\right) + \frac{1}{r^2}\frac{\partial^2 q_r}{\partial \theta^2} + \frac{\partial^2 q_r}{\partial z^2} - \frac{2}{r}\frac{\partial q_\theta}{\partial \theta}\right], \\
\frac{Dq_z}{Dt} &= -\frac{\partial p}{\partial z} + \frac{1}{Re}\left[\frac{1}{r}\frac{\partial}{\partial r}\left(r\frac{\partial q_z}{\partial r}\right) + \frac{1}{r^2}\frac{\partial^2 q_z}{\partial \theta^2} + \frac{\partial^2 q_z}{\partial z^2}\right],
\end{aligned} \tag{2}$$

with

$$\begin{aligned}
\frac{Dq_\theta}{Dt} &= \frac{\partial q_\theta}{\partial t} + \frac{1}{r}\frac{\partial q_\theta q_r}{\partial r} + \frac{q_\theta q_r}{r^2} + \frac{1}{r}\frac{\partial q_\theta^2}{\partial \theta} + \frac{\partial q_\theta q_z}{\partial z}, \\
\frac{Dq_r}{Dt} &= \frac{\partial q_r}{\partial t} + \frac{\partial}{\partial r}\left(\frac{q_r^2}{r}\right) + \frac{\partial}{\partial \theta}\left(\frac{q_\theta q_r}{r}\right) + \frac{\partial q_r q_z}{\partial z} - q_\theta^2, \\
\frac{Dq_z}{Dt} &= \frac{\partial q_z}{\partial t} + \frac{1}{r}\frac{\partial q_r q_z}{\partial r} + \frac{1}{r}\frac{\partial q_\theta q_z}{\partial \theta} + \frac{\partial q_z^2}{\partial z}.
\end{aligned} \tag{3}$$

All the variables are non-dimensionalized by a characteristic length (δ) and velocity scale (U_m) and Re is the Reynolds number. A numerical method in cylindrical coordinates requires a large effort to treat the singularity at $r = 0$. In the present formulation, the quantity $q_r = rv_r$ on a staggered grid is introduced to simplify the discretization of this region since $q_r = 0$ at $r = 0$ (Verzicco and Orlandi, 1996).

The governing equations (1) and (2) are integrated in time by using a fractional step method with an implicit velocity decoupling procedure, which has been proposed by Kim et al. (2002). After all the terms are discretized with the Crank–Nicolson method in time, the coupled velocity components in the convection terms are decoupled by the implicit velocity decoupling procedure. Decoupled velocity components are solved without iteration. Since the implicit decoupling procedure relieves the CFL restriction, the computational time is reduced significantly. The overall accuracy in time is sec-

ond-order. All the terms are resolved with a second-order central difference scheme in space with a staggered mesh. Details regarding the numerical algorithm are available in Kim et al. (2002).

Periodic boundary conditions for velocity components are applied in the axial and circumferential directions. A no-slip boundary condition is imposed at the solid wall. As for the computational domain, a full domain of the concentric annular pipe is chosen for $\alpha = 0.1$. However, the computation is conducted in only one-quarter of the full cross-section for $\alpha = 0.5$. Note that the computational length in the streamwise direction is $L_z = 18\delta$ for $\alpha = 0.5$ and $L_z = 15\delta$ for $\alpha = 0.1$, respectively. To illustrate the adequacy of the computational domains, two-point correlations of the fluctuating streamwise velocities in the streamwise (z) and azimuthal (θ) directions are shown in Figs. 2 and 3. For

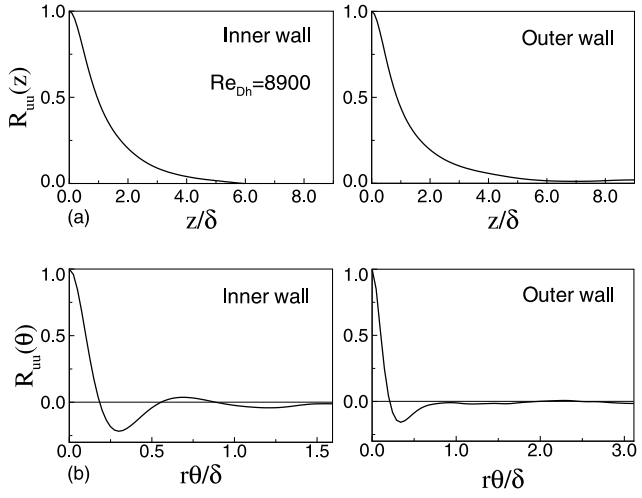

Fig. 2. Two-point correlation coefficients for $\alpha = 0.5$: (a) streamwise separations and (b) azimuthal separations.

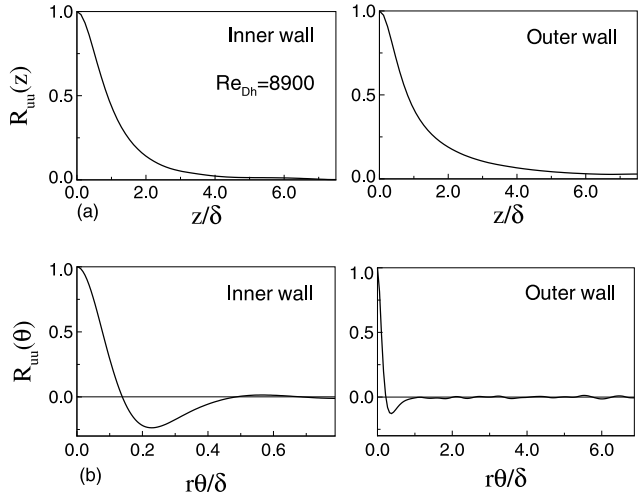

Fig. 3. Two-point correlation coefficients for $\alpha = 0.1$: (a) streamwise separations and (b) azimuthal separations.

Table 1
Grid resolutions

α	0.5	0.1
L_z^+	2746.80	2688.75
$L_{\theta_i}^+$	479.50	250.28
$L_{\theta_o}^+$	909.25	1975.57
Δz^+	14.30	14.00
$(R_1\Delta\theta)^+$	3.75	0.98
$(R_2\Delta\theta)^+$	7.10	7.72
Δr_i^+	0.13	0.15
Δr_o^+	0.12	0.12
Δr_{max}^+	12.96	15.23
(N_r, N_θ, N_z)	(65,128,192)	(65,256,192)

$\alpha = 0.5$, the two-point correlations in Fig. 2 show that they fall off to zero values for separations. For $\alpha = 0.1$, similar trends of the correlations are shown in Fig. 3. This suggests that the computational domains are sufficiently large for both cases. The detailed grid resolutions for two cases are listed in Table 1. As mentioned earlier, two values of α (= 0.1 and 0.5) are chosen for computations. These exemplify the situations in which the curvature effect, compared to the overall curvature effects of turbulent channel and pipe flows, is strong and weak, respectively. The computational time step used is $0.04\delta/U_c$ and the total averaging time to obtain the statistics is $600\delta/U_c$ for both cases. Here, U_c is the laminar maximum velocity. A hyperbolic tangent distribution is used for a clustering of grid points in the wall-normal direction.

3. Results and discussion

3.1. Mean flow properties

Before proceeding further, it is important to ascertain the reliability and accuracy of the present numerical simulation. Toward this end, a comparison is made of the mean velocity distributions normalized by the bulk velocity with the experimental data of Nouri et al. (1993) as shown in Fig. 4(a). Agreement with the experimental data is satisfactory, although a slight deviation is observed in the center region. It is interesting to note that the integration of the measured profiles in the radial direction does not yield a value of unity while that of the numerical profiles shows 1.0. This tendency was also pointed out in the previous numerical investigation (Azouz and Shirazi, 1998). When rescaled by a process of normalization, the numerical prediction is in excellent agreement with the experimental data. Note that the positions of the maximum velocities are skewed toward the inner wall in both cases. Several mean flow parameters obtained from the present simulation are summarized in Table 2. Here, Re_δ is based on the laminar maximum velocity (U_c) and the half width (δ) between the inner and outer walls. In Table 2, the skin friction

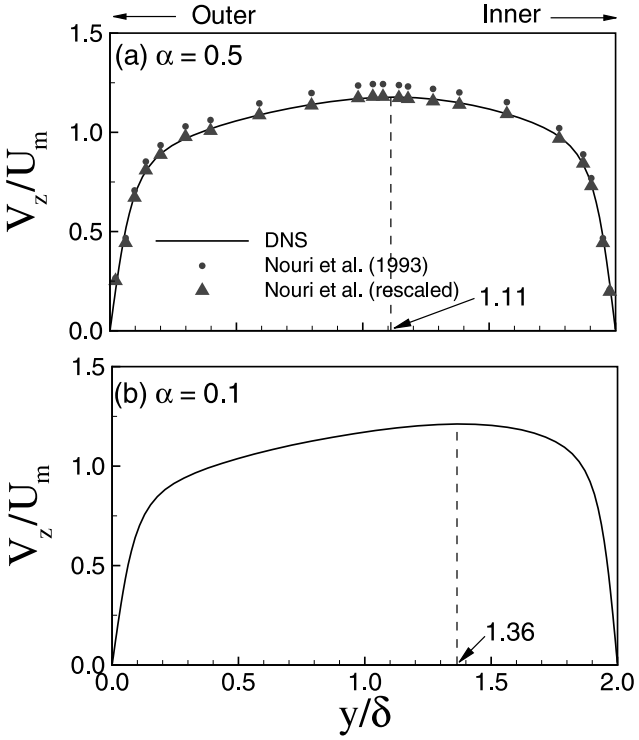

Fig. 4. Mean velocity distributions.

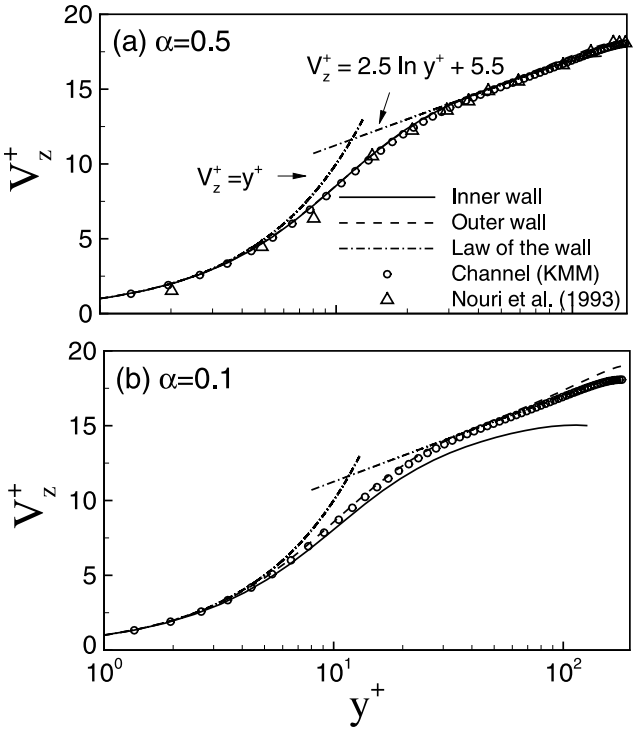

Fig. 5. Mean velocity distributions for the law of the wall.

Table 2
Mean flow parameters

α	0.5	0.1
Re_{D_h}	8900	8900
Re_δ	3355	3487
Re_τ (Inner)	153	179
Re_τ (Outer)	144	141
C_f (Inner)	0.00941	0.01300
C_f (Outer)	0.00849	0.00810
$-K_p$ (Inner)	0.00380	0.00242
$-K_p$ (Outer)	0.00449	0.00492
U_c/u_τ (Inner)	22.09	19.45
U_c/u_τ (Outer)	23.26	24.65
U_m/u_τ (Inner)	14.65	12.41
U_m/u_τ (Outer)	15.43	15.72

coefficient ($C_f = \tau_w/(1/2)\rho U_m^2$) of the inner wall is larger than that of the outer wall. Moreover, this tendency becomes more clear as α decreases. The value of C_f according to the empirical relation of Nouri et al. (1993) $C_f = 0.36Re^{-0.39}$ is 0.01038 for $\alpha = 0.5$ and $Re = 8900$. In the present study, the skin friction coefficient based on the averaged friction velocity $C_f = (R_i/(R_i + R_o))C_{f_i} + (R_o/(R_i + R_o))C_{f_o}$ is 0.0088 for $\alpha = 0.5$. This value is smaller than that of Nouri et al. (1993). The values of non-dimensional pressure gradient $K_p = \nu/(\rho u_\tau^3)\,\mathrm{d}p/\mathrm{d}z$ are listed in Table 2 (Patel, 1965). Note that the value $-K_p$ of outer wall is larger than that of inner wall.

Comparison is extended to the logarithmic velocity profiles in Fig. 5. In Fig. 5(a), a slight discrepancy between the profiles of the inner and outer walls appears only in the region of $y^+ > 100$. In Fig. 5(b), however, the deviations are significant and the slope of the inner profile is lower than that of the outer profile in the logarithmic region. This may be attributed to the curvature effect, which is caused by the decrease of the radius of the inner cylinder.

3.2. Turbulent intensities and Reynolds shear stresses

R.m.s. distributions of the fluctuating velocities, normalized by the friction velocity (u_τ), are exhibited in Fig. 6. A comparison between the inner and outer walls indicates that turbulent intensities of the inner wall are smaller than those of the outer wall. This tendency is pronounced at $\alpha = 0.1$. The smaller turbulent kinetic energy in the inner wall is due to the transverse curvature effect. Since the surface area of the inner wall is smaller than that of the outer wall, the inner wall supplies relatively less turbulent kinetic energy than the outer wall to the same volume of flow.

To examine the altered energy redistributions by the curvature effect, the energy partition parameter $K^* = (2\overline{v_z'^2}/(\overline{v_r'^2} + \overline{v_\theta'^2}))$ is employed (Lee et al., 1990) and the results are shown in Fig. 7. This is a measure of the relative contribution to the turbulent kinetic energy of the streamwise turbulence intensity and the intensities normal to the mean flow (Neves et al., 1994). It is seen that the values of K^* near the inner wall are larger than those near the outer wall in the region $y^+ < 60$. This

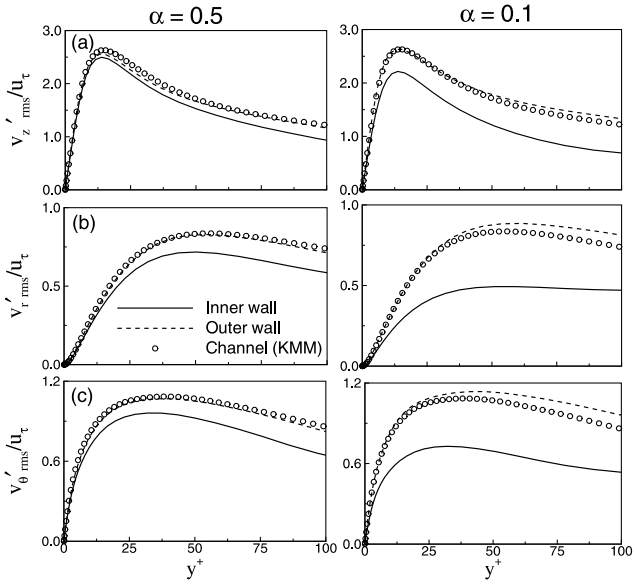

Fig. 6. R.m.s. velocity fluctuations: (a) axial velocity, (b) normal velocity and (c) azimuthal velocity.

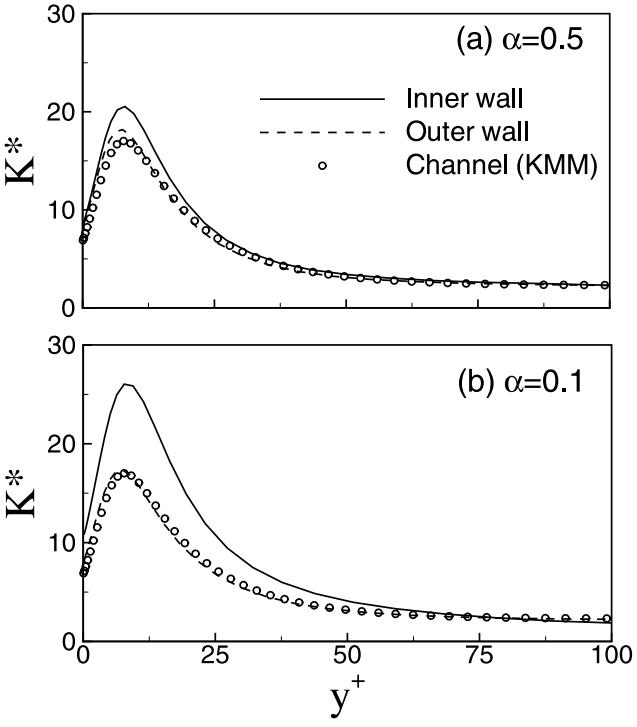

Fig. 7. Energy partition parameter $K^* = 2\overline{v_z'^2}/(\overline{v_r'^2} + \overline{v_\theta'^2})$.

suggests that the amount of energy transfer from the streamwise velocity component to the other two velocity components near the inner wall is smaller than that near the outer wall.

The Reynolds shear stress $(-\overline{v_z'v_r'})$ and total shear stress $(-\overline{v_z'v_r'} + (1/Re)(\mathrm{d}V_z/\mathrm{d}y))$ in the global coordinate are shown in Fig. 8(a). Here, y and v_r denote a distance

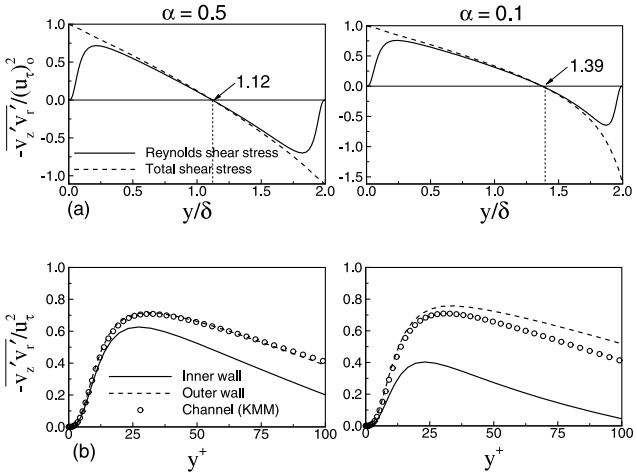

Fig. 8. Distributions of Reynolds shear stress and total shear stress.

from the outer wall and a velocity component normal to the outer wall, respectively. In Fig. 8(a), distributions of the Reynolds shear stress and total shear stress are asymmetric, similar to those of the mean velocities in Fig. 4. It is interesting to note that the positions of zero total shear stresses are closer to the inner walls than those of the maximum velocities (see Fig. 4). This phenomenon is also demonstrated in the experimental study of Rehme (1974). Furthermore, the distributions of the total shear stresses are slightly curvilinear due to the curvature, while these are linear in pipe and channel flows. Profiles of the Reynolds shear stress in the wall coordinate are displayed in Fig. 8(b). This suggests that the Reynolds shear stress near the outer wall is larger than that near the inner wall like the r.m.s. distributions of fluctuating velocities in Fig. 6.

3.3. Reynolds stress budgets

DNS is of great help in obtaining the various terms in the budgets for the Reynolds-stress components explicitly. Computed Reynolds-stress budgets by DNS provide detailed information on the dynamical characteristics of turbulence such as PR, redistribution and DS of turbulent kinetic energy. The transport equations of the Reynolds stresses are derived from the Navier–Stokes equations by ensemble-averaging the equations, then deriving equations for the fluctuating stresses and ensemble-averaging these equations (Mansour et al., 1988). In the present study, the flow is homogeneous in the streamwise and azimuthal directions. The only non-zero mean velocity is the one in the axial direction and all derivatives of mean quantities in the axial and circumferential directions disappear. The remaining terms of the Reynolds-stress equations and the turbulent kinetic energy $k = (1/2)(\overline{v_r'^2} + \overline{v_\theta'^2} + \overline{v_z'^2})$ in cylindrical coordinates under consideration are as follows:

$\overline{v_r'^2}$-budget:

$$0 = \underbrace{2\overline{p'\frac{\partial v_r'}{\partial r}}}_{\text{PS}} \underbrace{-\frac{2}{Re}\left[\overline{\left(\frac{\partial v_r'}{\partial r}\right)^2} + \overline{\frac{1}{r^2}\left(\frac{\partial v_r'}{\partial \theta} - v_\theta'\right)^2} + \overline{\left(\frac{\partial v_r'}{\partial z}\right)^2}\right]}_{\text{DS}}$$
$$\underbrace{-2\frac{\partial(\overline{v_r'p'})}{\partial r}}_{\text{PD}} \underbrace{-\frac{1}{r}\frac{\partial(r\overline{v_r'^3})}{\partial r} + \frac{2}{r}\overline{v_r'v_\theta'^2}}_{\text{TD}}$$
$$\underbrace{+\frac{1}{Re}\left[\frac{1}{r}\frac{\partial}{\partial r}\left(r\frac{\partial\overline{v_r'^2}}{\partial r}\right) + \frac{2}{r^2}\left(\overline{v_\theta'^2} - \overline{v_r'^2}\right)\right]}_{\text{VD}}; \quad (4)$$

$\overline{v_\theta'^2}$-budget:

$$0 = \underbrace{\frac{2}{r}\overline{p'\left(\frac{\partial v_\theta'}{\partial \theta} + v_r'\right)}}_{\text{PS}}$$
$$\underbrace{-\frac{2}{Re}\left[\overline{\left(\frac{\partial v_\theta'}{\partial r}\right)^2} + \overline{\frac{1}{r^2}\left(\frac{\partial v_\theta'}{\partial \theta} + v_r'\right)^2} + \overline{\left(\frac{\partial v_\theta'}{\partial z}\right)^2}\right]}_{\text{DS}}$$
$$\underbrace{-\frac{2}{r}\overline{v_r'p'}}_{\text{PD}} \underbrace{-\frac{1}{r}\frac{\partial(r\overline{v_r'v_\theta'^2})}{\partial r} - \frac{2}{r}\overline{v_r'v_\theta'^2}}_{\text{TD}}$$
$$\underbrace{+\frac{1}{Re}\left[\frac{1}{r}\frac{\partial}{\partial r}\left(r\frac{\partial\overline{v_\theta'^2}}{\partial r}\right) - \frac{2}{r^2}\left(\overline{v_\theta'^2} - \overline{v_r'^2}\right)\right]}_{\text{VD}}; \quad (5)$$

$\overline{v_z'^2}$-budget:

$$0 = \underbrace{-2\overline{v_r'v_z'}\frac{\mathrm{d}V_z}{\mathrm{d}r}}_{\text{PR}} + \underbrace{2\overline{p'\frac{\partial v_z'}{\partial z}}}_{\text{PS}}$$
$$\underbrace{-\frac{2}{Re}\left[\overline{\left(\frac{\partial v_z'}{\partial r}\right)^2} + \overline{\frac{1}{r^2}\left(\frac{\partial v_z'}{\partial \theta}\right)^2} + \overline{\left(\frac{\partial v_z'}{\partial z}\right)^2}\right]}_{\text{DS}}$$
$$\underbrace{-\frac{1}{r}\frac{\partial(r\overline{v_r'v_z'^2})}{\partial r}}_{\text{TD}} + \underbrace{\frac{1}{Re}\left[\frac{1}{r}\frac{\partial}{\partial r}\left(r\frac{\partial\overline{v_z'^2}}{\partial r}\right)\right]}_{\text{VD}}; \quad (6)$$

k-budget:

$$0 = \underbrace{-\overline{v_r'v_z'}\frac{\mathrm{d}V_z}{\mathrm{d}r}}_{\text{PR}} \underbrace{-\epsilon}_{\text{DS}} \underbrace{-\frac{1}{r}\frac{\mathrm{d}}{\mathrm{d}r}(r\overline{v_r'p'})}_{\text{PD}} \underbrace{-\frac{1}{r}\frac{\mathrm{d}}{\mathrm{d}r}(r\overline{v_r'k})}_{\text{TD}}$$
$$\underbrace{+\frac{1}{Re}\left[\frac{1}{r}\frac{\mathrm{d}}{\mathrm{d}r}\left(r\frac{dk}{dr}\right)\right]}_{\text{VD}}. \quad (7)$$

Terms on the right-hand sides of (4)–(7) are identified as follows: PR, PS, PD, DS, TD and VD. The two pressure terms can be combined to form the VPG (Eggels et al., 1994). The PR terms in the turbulent kinetic energy budget are displayed in Fig. 9. It is shown that the positions of the maximum values are located at $y^+ \approx 12$ for both cases. This is consistent with the DNS results of turbulent channel and pipe flow (Mansour et al., 1988; Eggels et al., 1994). Note that the values of the outer walls are larger than those of the inner walls for both cases. This reconfirms the results of the r.m.s. profiles of fluctuating velocities in Fig. 6.

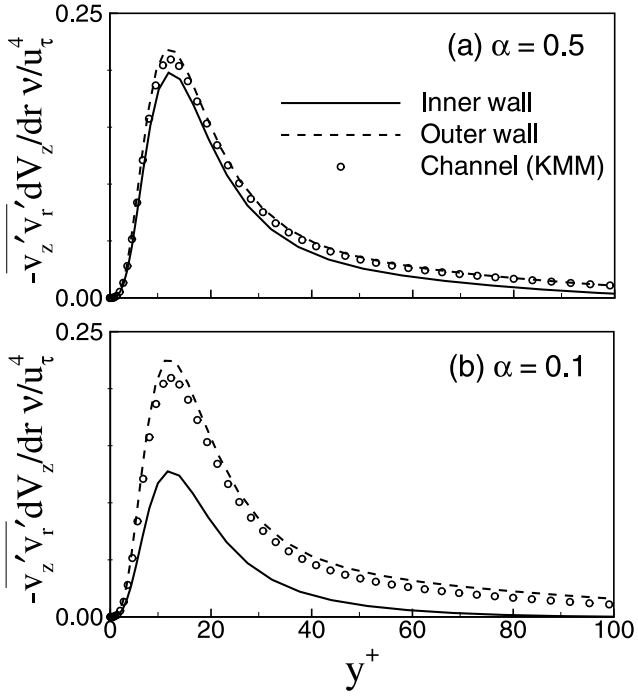

Fig. 9. PR terms in the budget of the turbulent kinetic energy in wall coordinates.

In the budget equations of the turbulent intensities, the PS terms are responsible for the intercomponent energy transfer. Fig. 10 shows the PS terms in Eq. (7). It is seen that the profiles of the outer wall are larger than those of the inner wall for both cases. This indicates a lower energy redistribution of the inner wall, which represents the same results as the energy partition parameter $K^* = (2\overline{v_z'^2}/(\overline{v_r'^2} + \overline{v_\theta'^2}))$ in Fig. 7.

3.4. Higher-order statistics

In this subsection, we consider the skewness and flatness factors of fluctuating velocities to explore the transverse curvature effect on higher-order statistics. To attain these quantities with high reliability, a larger statistical sample size is required than in the case of the second-order statistics. The sufficiency of satisfying this condition can be examined by evaluating the skewness factor of the fluctuating azimuthal velocities. Because of the reflective symmetry of the Navier–Stokes equations,

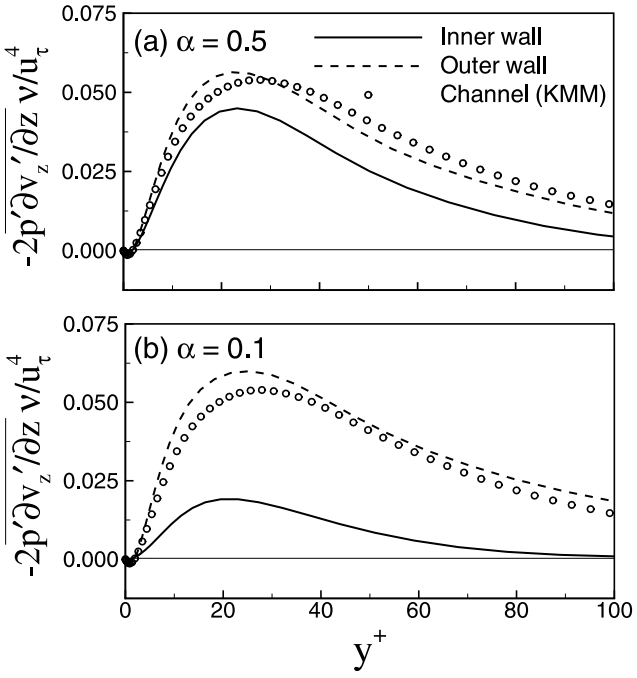

Fig. 10. PS terms in the budget of $\overline{v_z' v_z'}$ in wall coordinates.

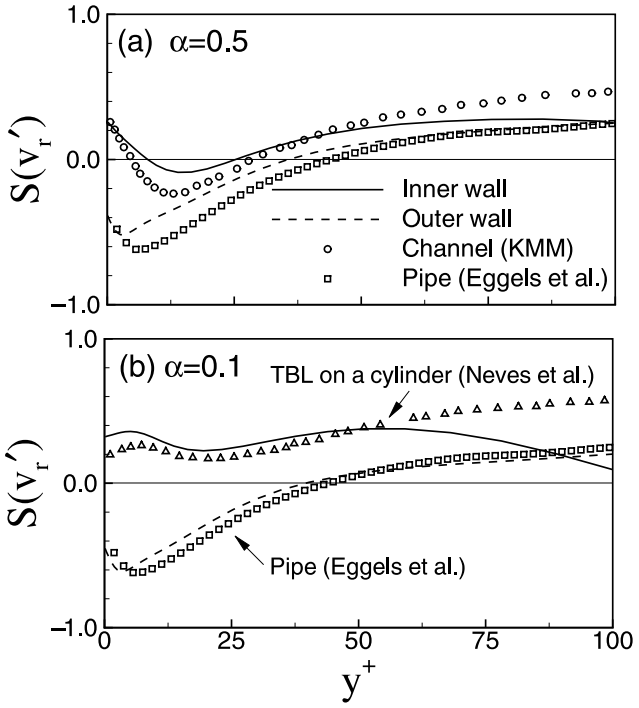

Fig. 11. Skewness profiles of the wall-normal velocity fluctuations.

the skewness of v_θ should equal zero everywhere. However, there are small oscillations around zero in the computed statistics (≈0.05 and 0.02 for $\alpha = 0.1$ and 0.5, respectively (not shown)). Although this is owing to the finite statistical sample, it is reasonable to believe that the present results are good when compared to those in the previous DNSs of pipe and channel flows (Eggels et al., 1994; Kim et al., 1987).

The skewness factors of the wall-normal velocity fluctuations are exhibited in Fig. 11. Here, wall-normal velocity v_r is defined to be positive in the direction outward from the wall. In Fig. 11(a), the skewness factor of the inner wall becomes zero at two points $y^+ \approx 7$ and $y^+ \approx 25$, in contrast to that of the outer wall which has only one crossover point at $y^+ \approx 35$. These results for the inner and outer walls are consistent with the previous numerical data for channel and pipe flows corresponding to the inner and outer walls, respectively (Kim et al., 1987; Eggels et al., 1994). In the region of $y^+ > 50$, there is a large discrepancy between the profiles of the inner wall and channel flow. This is because the value of zero-shear point ($y^+ \approx 130$) of the inner wall is smaller than that of the channel flow ($y^+ \approx 180$). In Fig. 11(b), the profile of the skewness factor near the outer wall is similar to that in the pipe flow. Near the inner wall, however, the profile is positive throughout the layer. This tendency is discernible in the numerical simulation of TBL on a cylinder in an axial flow (Neves et al., 1994). A large difference is also observed between the profiles of the inner wall and the TBL on a cylinder as in the case of $\alpha = 0.5$. An examination of the results in Fig. 11 indicates that the concentric annular pipe flow has the general characteristics of fully developed flows such as channel and pipe flows. Furthermore, for a small radius ratio ($\alpha = 0.1$), the turbulent structure near the inner wall is similar to that of the external flow longitudinal to a cylinder. One could think about a difference between the wall-bounded and the external flows, e.g., a plane channel flow and a TBL. This can be observed in a zero-shear region of the wall-bounded flow and a non-turbulent free stream region of the external flow. The r.m.s. values of velocity fluctuations in a turbulent plane channel flow and a TBL are a good example (Pope, 2000). In the inner layer of the TBL, the r.m.s. profiles are almost similar to those in the channel flow. As the edge of the boundary layer is approached, the r.m.s. values tend to zero. Near the zero-shear region of the channel flow, however, the r.m.s. values exhibit non-zero ones.

To explain the altered intermittent behavior of the inner and outer walls, which is pertinent to the subsequent interpretation of the PR of Reynolds shear stress, the flatness factors of the wall-normal velocity fluctuations are shown in Fig. 12. For $y^+ > 25$, the flatness factors are only a little larger than the corresponding value for a Gaussian distribution ($F = 3$). Near the wall ($y^+ < 20$), the values of the flatness factor near the inner and outer walls rapidly increase for both cases. This reflects the high intermittency of the wall-normal velocity fluctuations close to the wall. As reported in the numerical simulation of Xu et al. (1996), such high

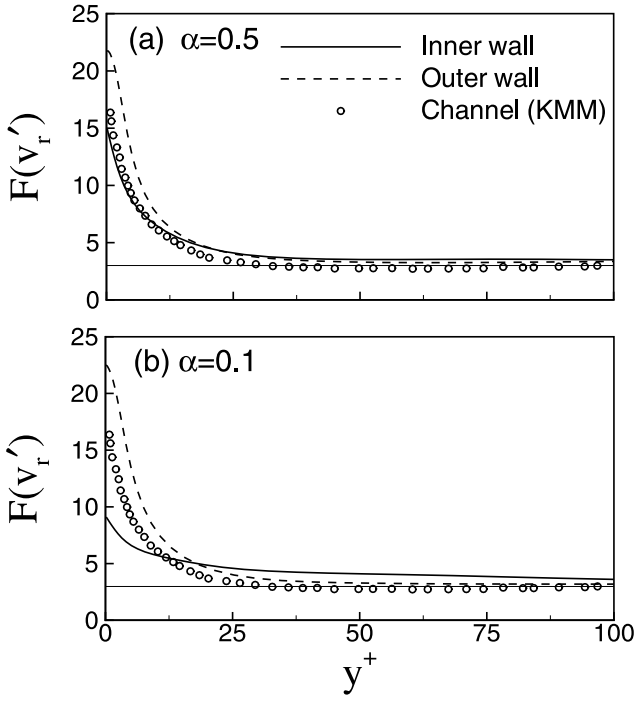

Fig. 12. Flatness profiles of the wall-normal velocity fluctuations.

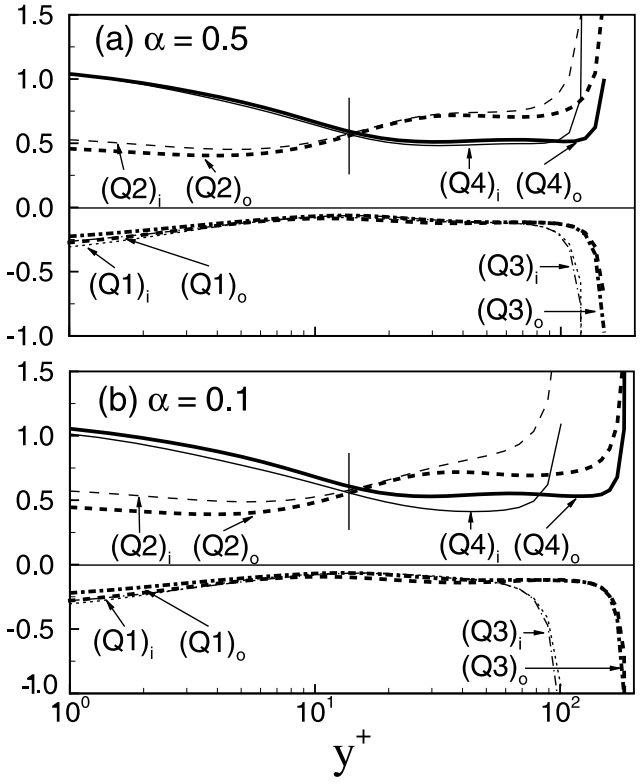

Fig. 13. Reynolds shear stress for each quadrant normalized by the mean Reynolds shear stress.

values are attributed to strong sweep events. Note that the outer profiles are larger than the inner profiles in the vicinity of the walls for both cases. As a result, the sweep events in the outer walls may be stronger than those in the inner walls. To manifest this phenomenon, a quadrant analysis for the Reynolds shear stresses is carried out in Section 3.5.

3.5. Quadrant analysis

The quadrant analysis of the Reynolds shear stress provides detailed information on the contribution of flow events to the PR (consumption) of the turbulent kinetic energy (Brodkey et al., 1974; Willmarth and Lu, 1972). The analysis divides the Reynolds shear stress into four categories according to the signs of u' and v'. The Q1, $u' > 0$ and $v' > 0$, contains outward motion of high-speed fluid; the Q2, $u' < 0$ and $v' > 0$, contains outward motion of low-speed fluid referred to as the ejection events; the Q3, $u' < 0$ and $v' < 0$, contains inward motion of low-speed fluid; the Q4, $u' > 0$ and $v' < 0$, contains an inrush of high-speed fluid referred to as the sweep events. Here, Q1 and Q3 events contribute to the positive Reynolds shear stress (negative production), and Q2 and Q4 events contribute to the negative Reynolds shear stress (positive production).

The contribution to the Reynolds shear stress from each quadrant is shown in Fig. 13. The thin and thick lines denote the profiles of the inner wall and outer wall, respectively. The crossover points between the dominance of Q2 and Q4 events are located at $y^+ \approx 13$ for both cases. This is very similar to the numerical results for the channel and TBL on a cylinder in an axial flow (Neves et al., 1994; Kim et al., 1987). When we compare the inner and outer profiles, it is notable that sweep events near the outer walls are more predominant than those near the inner walls. On the other hand, ejections near the inner walls contribute to the Reynolds shear stress more predominantly than those near the outer walls. This can be interpreted to be the same result as that of the flatness factors of wall-normal velocity fluctuations in Section 3.4. However, since the quadrant analysis provides not only the strength of sweep events but also the number of occurrences of sweep events, more detailed investigations are required to assess the effects of the strength of sweep events solely.

To explain the difference in the strength of sweep events between inner and outer walls more clearly, scatter plots of the instantaneous u' and v' for $\alpha = 0.1$ are illustrated in Figs. 14 and 15. Six y-locations are selected to show the altered dominance of sweep and ejection events around the crossover point, which is confirmed in Fig. 13. At $y^+ = 2, 5$ and 8, sweep motions are more dominant than ejections. At the crossover point ($y^+ = 13$), sweep and ejection events seem to be the same as each other. Further away from the wall ($y^+ = 20$ and 50), ejections are more distinct than sweep motions. In Figs. 14 and 15, it should be noted that

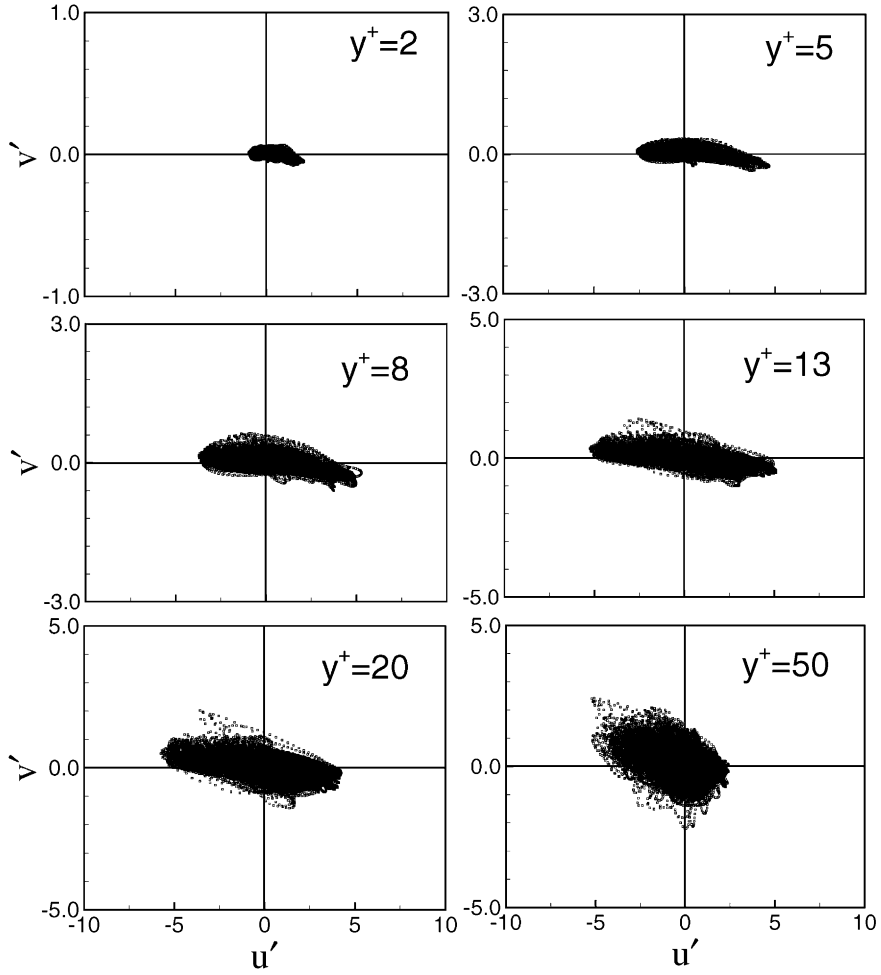

Fig. 14. Instantaneous distributions of (u', v') near the inner wall for $\alpha = 0.1$.

sweep events near the outer wall are much stronger than those near the inner wall. This guarantees that the strength of the sweep motions near the outer wall is higher than that near the inner wall.

Instantaneous contours of $-v_r'v_z'$ and velocity vectors in a r–θ plane are depicted in Figs. 16 and 17. The dark and bright regions reflect negative and positive Reynolds shear stress near the inner wall, respectively. In the case of the outer wall, the sign of Reynolds shear stress according to the brightness is opposite to that in the case of the inner wall. Strong sweep and ejection events can be observed near the inner and outer walls where the Reynolds shear stress is high. These figures further illustrate the point discussed above that the fluid particles entailing strong sweep motions near the outer wall are detected more frequently than those near the inner wall.

As discussed above, it can be clearly seen that the turbulent structures near the outer wall are more activated than those near the inner wall. This may be attributed to the different vortex regeneration processes between the inner and outer wall. Brooke and Hanratty (1993) and Bernard et al. (1993) stated that flow-oriented vortices in the near-wall region can create other streamwise vortices through strong sweep motions. In the present turbulent concentric annular pipe considered here, the vortex regeneration process near the outer wall may occur more violently than near the inner wall, since the surface area of the outer wall with which the streamwise vortex can interact is larger than that of the inner wall. However, further detailed investigations should be implemented to clarify the different turbulent structures between the inner and outer walls.

3.6. Vorticity

It is known that vorticity is closely related to turbulence PR and sustenance in a wall-bounded turbulent flow. We now develop a dynamical explanation for the different turbulent structures between the inner and outer walls by scrutinizing vorticity. Vorticity fluctuations normalized by the mean wall shear stress are shown in Fig. 18. For both cases ($\alpha = 0.1$ and 0.5), all the vorticity intensities near the inner walls are lower than those near the outer walls, except for the

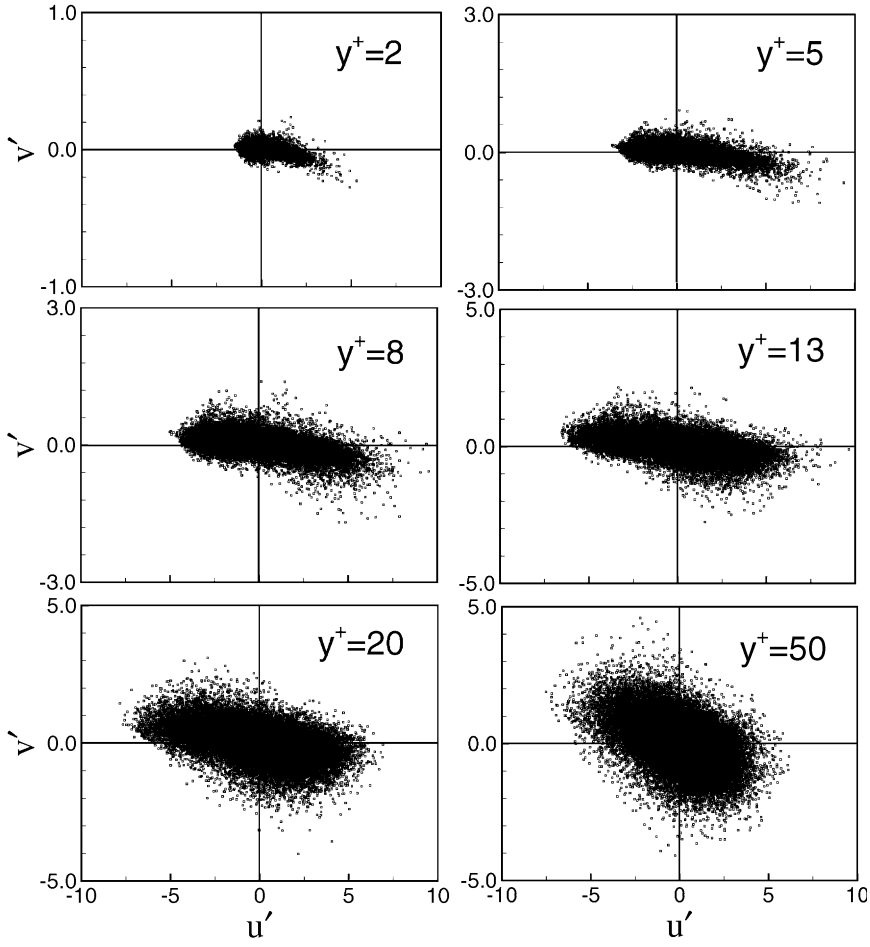

Fig. 15. Instantaneous distributions of (u', v') near the outer wall for $\alpha = 0.1$.

wall-normal vorticity intensities which are unaffected by the curvature near the walls ($y^+ < 10$). In Fig. 18, the axial vorticity intensity exhibits a near-wall local minimum at $y^+ = 5$ and a local maximum at $y^+ = 20$ regardless of the curvature. This is consistent with the result of Kim et al. (1987), where they linked the loca-

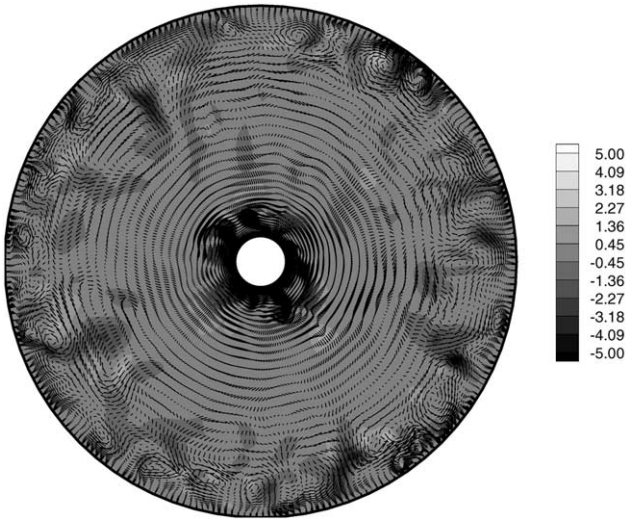

Fig. 16. Instantaneous contours of $-v_r'v_z'$ and vector plots in a r–θ plane for $\alpha = 0.1$.

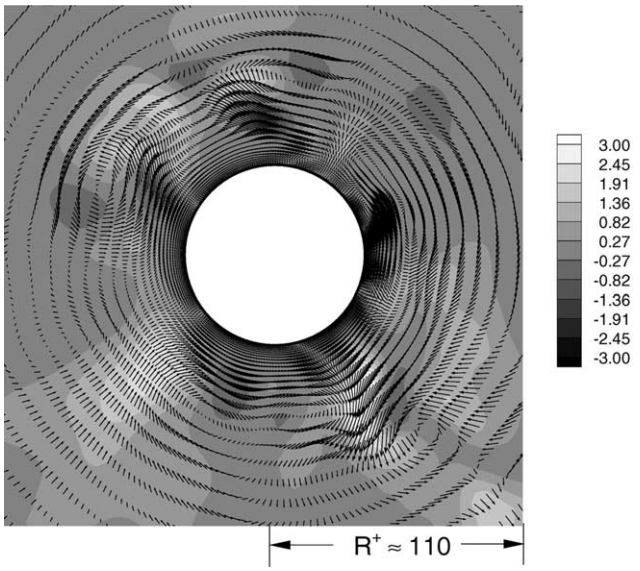

Fig. 17. Enlarged instantaneous contours of $-v_r'v_z'$ and vector plots in a r–θ plane for $\alpha = 0.1$.

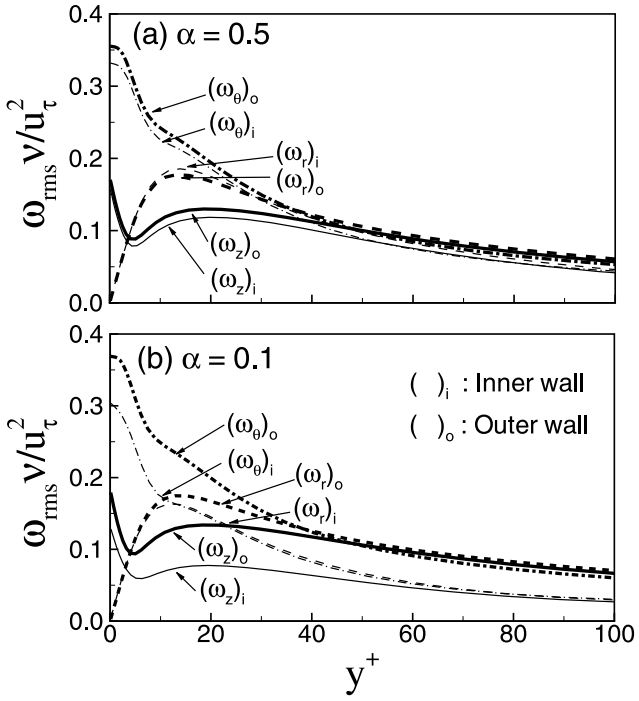

Fig. 18. R.m.s. vorticity fluctuations.

tions and intensity of these extrema to the average position and strength of the near-wall streamwise vortices. As in the simulation of TBL on a cylinder in an axial flow (Neves et al., 1994), both the streamwise vortex core radius and the position of the center of these vortices are not changed appreciably with curvature, although the strength of the vortices is greatly reduced.

To obtain a better understanding of the transverse curvature effect on the vorticity, a statistical investigation on the orientation of the vorticity field is made. Here, we follow the approach of Moin and Kim (1985). The inclination of the projection of the vorticity vector in a r–z plane is given by

$$\Theta = \tan^{-1}\left(\frac{\omega_r}{\omega_z}\right). \tag{8}$$

The p.d.f.s of Θ, weighted by the magnitude of the projected vorticity vector $(\omega_r^2+\omega_z^2)/\langle\omega_r^2+\omega_z^2\rangle$, are shown in Figs. 19 and 20. Here, $\langle\ \rangle$ indicates the mean of the quantity inside the brackets taken on the corresponding z–θ plane. The weighted p.d.f.s described below enhance the contributions of the strong vorticity fluctuations. At the closest point to the walls ($y^+ \approx 0.7$), the distributions are highly concentrated around 0° and ±180°. This is because the wall-normal vorticity is zero due to no-slip. As one moves away from the wall, the peaks of the distributions are located around ±90°. This tendency persists up to $y^+ \approx 16$ and 37 in Fig. 19(a) and (b), respectively and up to $y^+ \approx 10$ in Fig. 20. Further from the wall, the peak shifts to −135° and 45° as was observed by Moin and Kim (1985). Note that there exists a thicker layer near the outer wall, in which the vorticity has a −135° and 45° orientation. This suggests that the vortical structures inclined at 45° to the mean flow in the outer wall occur more frequently.

Turbulent energy of eddies has to be sustained by the shear flow, since the energy is continuously transferred to smaller eddies. In other words, the energy transfer from large eddies to small eddies can be considered in terms of a vortex stretching mechanism. The eddies which are more effective than others in absorbing energy from the mean flow are vortices whose principal axis is aligned with that of the mean strain rate (Tennekes and Lumley, 1972). For the concentric annular pipe flow considered in the present study, the principal axis of the mean strain rate tensor S_{ij} is inclined at 45° to the flow direction. This fact suggests that the vortices which can extract turbulent energy from the mean flow effectively are observed more frequently near the outer wall as was shown in Figs. 19 and 20. The strength of vortices is increased by vortex stretching owing to the conservation of angular momentum. Thus, strong evidence for the discrepancy between the inner and outer profiles in Fig. 18 can be obtained by explaining the vortex stretching mechanism. In addition, since this stretching mechanism by the mean shear enhances the correlation between u' and v', the differences in the Reynolds shear stress discussed previously can be understood well in light of this phenomenon.

4. Conclusions

A detailed numerical analysis has been performed to delineate the transverse curvature effects on near-wall turbulent structures in a turbulent concentric annular pipe flow. The statistical descriptions of the turbulent quantities were obtained by performing a DNS of turbulent concentric annular pipe flow at $Re_{D_h} = 8900$ for two radius ratios ($\alpha = 0.1$ and 0.5). In the first place, the mean velocity distribution normalized by the bulk velocity for $\alpha = 0.5$ was represented to validate the present simulation. The mean velocity distribution was in good agreement with the previous experimental results. It was obvious from the mean velocity distributions that a distinctive feature of concentric annular pipe flow is the radial asymmetry of the statistics—the smaller the radius ratio, the more asymmetric the flow. It was found that the slope of the inner profile is lower than that of the outer profile in the logarithmic region.

Turbulent intensities and Reynolds shear stresses of the inner wall were smaller than those of the outer wall. Since the surface area of the inner wall is smaller than that of the outer wall, the inner wall supplies relatively less turbulent kinetic energy than the outer wall to the same volume. From the investigation of the energy partition parameter, the intercomponent energy transfer

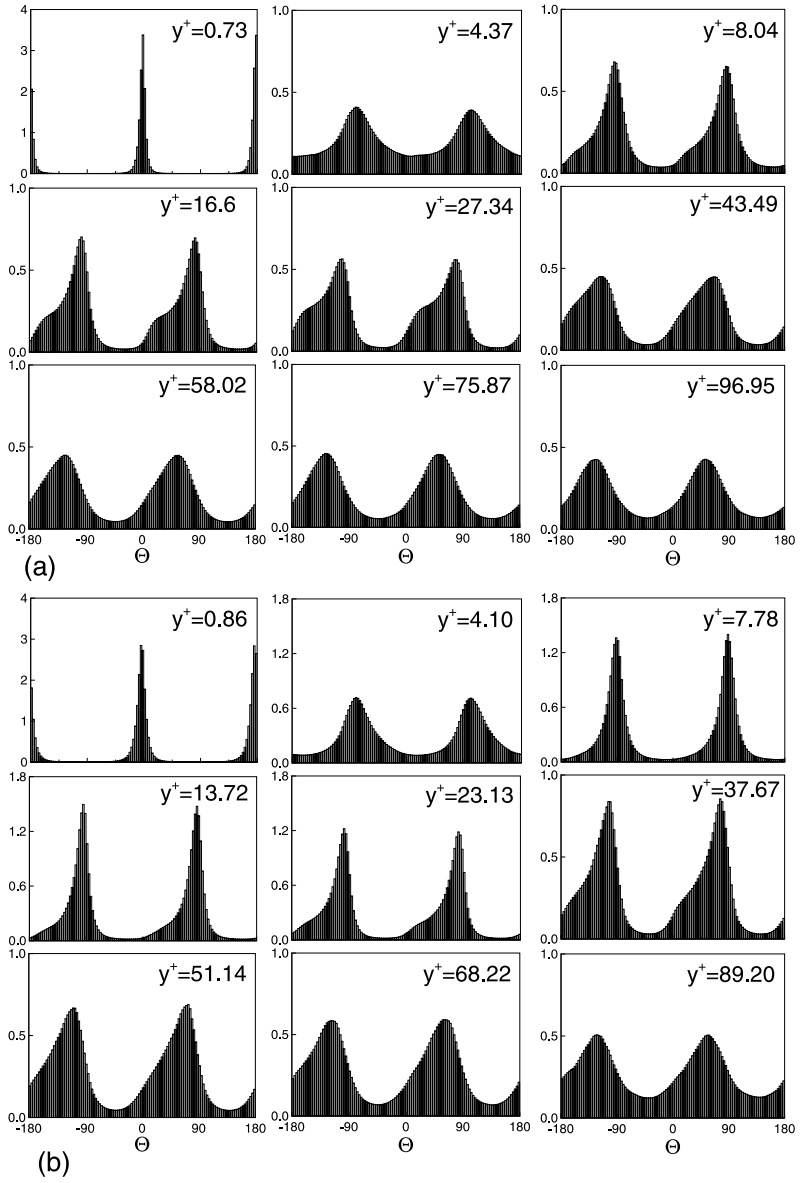

Fig. 19. Weighted p.d.f.s of the inclination angles of the projected vorticity vectors near the inner wall: (a) $\alpha = 0.5$ and (b) $\alpha = 0.1$.

in the inner wall was lower than that of the outer wall. This was confirmed by evaluating the PS terms of the streamwise intensity in the Reynolds stress budget analysis. More distinctive features of transverse curvature effects were represented in the higher-order statistics. The skewness factor of wall-normal velocity fluctuations indicated that the concentric annular pipe flow has the general characteristics of fully developed flows such as channel and pipe flows. The flatness factor of wall-normal velocity fluctuations reflected that the sweep events in the outer walls are stronger than those in the inner walls.

Detailed investigations on Reynolds shear stress and vorticity, which are directly associated with turbulence PR and maintenance, were accomplished. The quadrant analysis of Reynolds shear stress informed that the strength of the sweep events near the outer wall is greater than that near the inner wall. All the vorticities near the outer wall were higher than those of the inner wall, except for the wall-normal vorticity which was not affected near the wall ($y^+ < 10$). The average location and the radius of the streamwise vortices were consistent with the streamwise vortex model suggested by Kim et al. (1987). From the p.d.f.s of the inclination angles of the projected vorticity vectors, the transverse curvature effects on the orientation of the vorticity field were explored. This suggested that the vortices which can extract turbulent energy from the mean flow most effectively occur more frequently near the outer wall. The differences in the Reynolds shear stresses and the vorticity intensities between the inner and outer walls were also clarified by vortex stretching mechanisms.

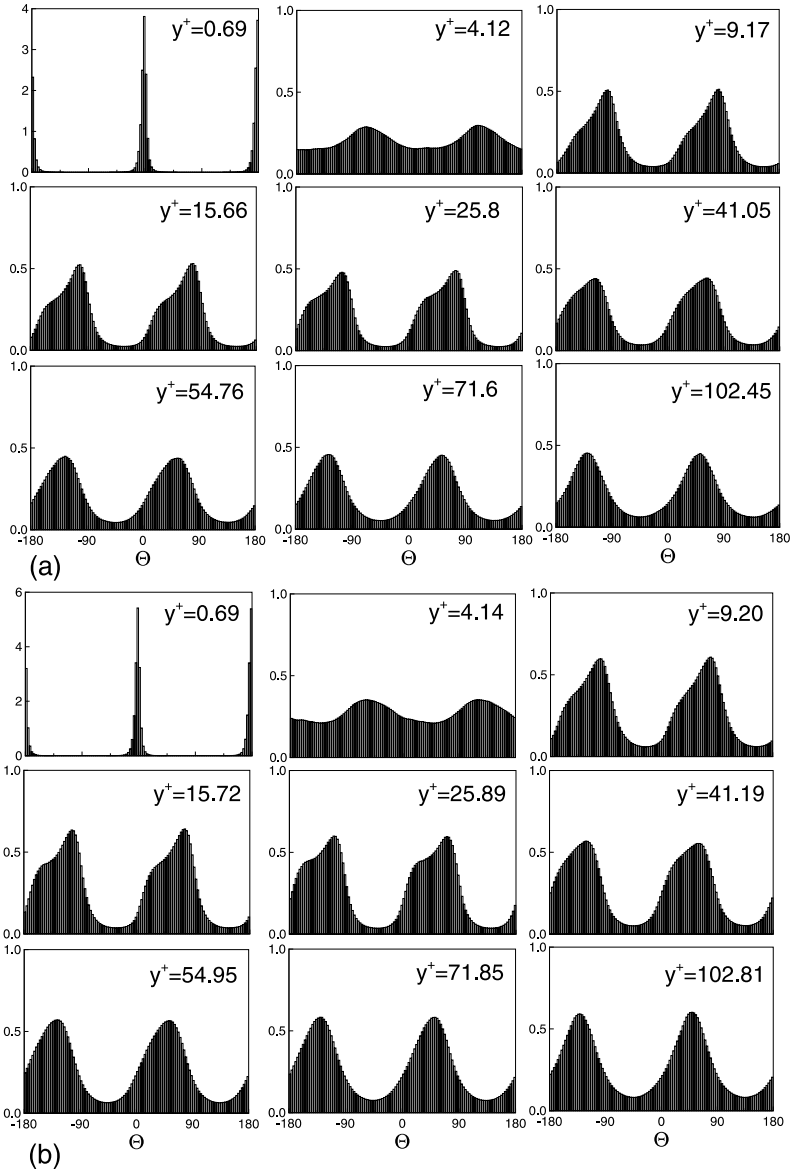

Fig. 20. Weighted p.d.f.s of the inclination angles of the projected vorticity vectors near the outer wall: (a) $\alpha = 0.5$ and (b) $\alpha = 0.1$.

Acknowledgements

This work was supported by a grant from the National Research Laboratory of the Ministry of Science and Technology, Korea.

References

Azouz, I., Shirazi, S.A., 1998. Evaluation of several turbulence models for turbulent flow in concentric and eccentric annuli. ASME J. Energy Resour. Technol. 120, 268–275.

Bernard, P.S., Thomas, J.M., Handler, R.A., 1993. Vortex dynamics and the production of Reynolds stress. J. Fluid Mech. 253, 385–419.

Brighton, J.A., Jones, J.B., 1964. Fully developed turbulent flow in annuli. J. Basic Engng. 86, 835–844.

Brodkey, R.S., Wallace, J.M., Eckelmann, H., 1974. Some properties of truncated turbulence signals in bounded shear flows. J. Fluid Mech. 63, 209–224.

Brooke, J.W., Hanratty, T.J., 1993. Origin of turbulence-producing eddies in a channel flow. Phys. Fluids 5, 1011–1022.

Eggels, J.G.M., Unger, F., Weiss, M.H., Westerweel, J., Adrian, R.J., Friedrich, R., Nieuwstadt, F.T.M., 1994. Fully developed turbulent pipe flow: a comparison between direct numerical simulation and experiment. J. Fluid Mech. 268, 175–209.

Escudier, M.P., Gouldson, I.W., Jones, D.M., 1995. Flow of shear-thinning fluids in a concentric annulus. Exp. Fluids 18, 225–238.

Jonsson, V.K., Sparrow, E.M., 1966. Experiments on turbulent-flow phenomena in eccentric annular ducts. J. Fluid Mech. 25, 65–86.

Kim, J., Moin, P., Moser, R., 1987. Turbulence statistics in fully developed channel flow at low Reynolds number. J. Fluid Mech. 177, 133–166.

Kim, K., Baek, S.-J., Sung, H.J., 2002. An implicit velocity decoupling procedure for the incompressible Navier–Stokes equations. Int. J. Numer. Meth. Fluids 38, 125–138.

Knudsen, J.G., Katz, D.L., 1950. Velocity profiles in annuli. In: Proceedings of Midwestern Conference on Fluid Dynamics, pp. 175–203.

Lee, M.J., Kim, J., Moin, P., 1990. Structure of turbulence at high shear rate. J. Fluid Mech. 216, 561–583.

Mansour, N.N., Kim, J., Moin, P., 1988. Reynolds-stress and dissipation-rate budgets in a turbulent channel flow. J. Fluid Mech. 194, 15–44.

Moin, P., Kim, J., 1985. The structure of the vorticity field in turbulent channel flow. Part 1: Analysis of instantaneous fields and statistical correlations. J. Fluid Mech. 155, 441–464.

Neves, J.C., Moin, P., Moser, R.D., 1994. Effects of convex transverse curvature on wall-bounded turbulence. Part 1: The velocity and vorticity. J. Fluid Mech. 272, 349–381.

Nouri, J.M., Umur, H., Whitelaw, J.H., 1993. Flow of Newtonian and non-Newtonian fluids in concentric and eccentric annuli. J. Fluid Mech. 253, 617–641.

Patel, V.C., 1965. Calibration of the Preston tube and limitations on its use in pressure gradients. J. Fluid Mech. 23, 185–208.

Pope, S.B., 2000. Turbulent Flows. Cambridge University Press, Cambridge.

Quarmby, A., 1967. An experimental study of turbulent flow through concentric annuli. Int. J. Mech. Sci. 9, 205–221.

Rehme, K., 1974. Turbulent flow in smooth concentric annuli with small radius ratios. J. Fluid Mech. 64, 263–287.

Satake, S., Kawamura, H., 1993. Large eddy simulation of turbulent flow in concentric annuli with a thin inner rod. In: Proceedings of the 9th Symposium on Turbulent Shear Flows, pp. 5.5.1–5.5.6.

Shin, D., Choi, H., 2000. Space-time characteristics of the wall shear stress fluctuations in a turbulent boundary layer with transverse curvature. In: Proceedings of the 8th European Turbulence Conference, pp. 459–462.

Tennekes, H., Lumley, J.L., 1972. A First Course in Turbulence. MIT Press, Cambridge.

Verzicco, R., Orlandi, P., 1996. A finite-difference scheme for three dimensional incompressible flows in cylindrical coordinates. J. Comput. Phys. 123, 402–414.

Willmarth, W.W., Lu, S.S., 1972. Structure of the Reynolds stress near the wall. J. Fluid Mech. 55, 65–92.

Xu, C., Zhang, Z., den Toonder, J.M.J., Nieuwstadt, F.T.M., 1996. Origin of high kurtosis levels in the viscous sublayer. Direct numerical simulation and experiment. Phys. Fluids 8, 1938–1944.